

Modeling photonic-crystal surface-emitting lasers by guided mode expansion: finite-size effects and higher-order modes

Downloaded from: https://research.chalmers.se, 2026-11-23 00:26 UTC

Citation for the original published paper (version of record):

Riedel, M., Persson, L., Apaydin, D. et al (2026). Modeling photonic-crystal surface-emitting lasers by guided mode expansion: finite-size effects and higher-order modes. Optics Express, 34(22): 40705-40724. http://dx.doi.org/10.1364/OE.603693

N.B. When citing this work, cite the original published paper.

research.chalmers.se offers the possibility of retrieving research publications produced at Chalmers University of Technology. It covers all kind of research output: articles, dissertations, conference papers, reports etc. since 2004. research.chalmers.se is administrated and maintained by Chalmers Library

(article starts on next page)

Research Article Vol. 34, No. 22 / 2 Nov 2026 / Optics Express 40705
Optics EXPRESS

Modeling photonic-crystal surface-emitting lasers by guided mode expansion: finite-size effects and higher-order modes

MORITZ RIEDEL,[1,*] LARS PERSSON,[2] DOĞUKAN APAYDIN,[2] ÅSA HAGLUND,[2] AND ULRICH THEODOR SCHWARZ[1]

[1] Institute of Physics, Chemnitz University of Technology, Chemnitz 09126, Germany
[2] Department of Microtechnology and Nanoscience, Chalmers University of Technology, Gothenburg 41296, Sweden
[*] moritz.riedel@physik.tu-chemnitz.de

Abstract: We investigate a three-dimensional simulation method for finite-sized photonic-crystal surface-emitting lasers (PCSELs) based on guided mode expansion (GME), which is capable of estimating lateral and vertical modal loss rates. The approach generalizes established three-dimensional coupled-wave theory (3D-CWT) by considering an arbitrarily large set of basis functions including higher-order lateral and vertical (waveguide) modes. Detailed comparisons between the two methods for a UV-C AlGaN PCSEL with a hexagonal lattice reveal corrections with respect to modal wavelengths and threshold gains. Furthermore, we demonstrate that interactions with higher-order waveguide modes, which can only be taken into account by GME, could enable the experimentally observed wide-angle lasing modes that distort the far-field.

© 2026 Optica Publishing Group under the terms of the Optica Open Access Publishing Agreement

1. Introduction

Photonic-crystal surface-emitting lasers (PCSELs) combine the single-mode operation in distributed-feedback lasers [1] with the vertical emission of symmetric beams as present in vertical-cavity surface-emitting lasers [2,3]. A two-dimensional photonic crystal (PC) layer gives rise to distributed in-plane feedback and coherent oscillations over large areas, enabling high output powers and small divergence angles [4]. Standing electromagnetic waves usually form at high-symmetry points of the resulting photonic band structure, such as the Γ point, with vanishing group velocities [5,6]. Furthermore, other Bragg refraction mechanisms mediated by the PC simultaneously lead to vertical outcoupling.

Recently, our groups including TU Berlin (see Acknowledgment) have demonstrated an optically pumped PCSEL comprising a hexagonal PC lattice that emits in the deep UV wavelength range near 275 nm [7]. Efficient and compact UV-C light sources with high brightness are desirable for a wide range of applications, including disinfection [8] and Raman spectroscopy [9].

In this work, we focus only on simulations of the electromagnetic fields, neglecting gain and intrinsic losses [10,11], which have been investigated using spatially dependent rate-equation models [12–15], which are capable of describing mode switching and spatial hole burning. Nevertheless, even numerical simulations considering only the electromagnetic modes cannot be performed without simplifications and approximations for realistically large PCSELs [16]. Generally, electromagnetic field simulations can be carried out by decomposing the simulation domain into smaller elements, which is performed in finite-difference time-domain (FDTD) or finite-element (FEM) methods [15,17,18]. On the other hand, solutions to Maxwell's equations can be expanded in a basis of coupled periodic functions, i.e., in reciprocal space, which can be particularly beneficial when dealing with periodic dielectric structures as those present in PCSELs. In contrast to real-space approaches, expansions in reciprocal space usually require fewer unknown variables, potentially leading to higher computational efficiency [19].

#603693 https://doi.org/10.1364/OE.603693
Journal © 2026 Received 27 Apr 2026; revised 22 Jul 2026; accepted 31 Aug 2026; published 19 Oct 2026

Optics EXPRESS

Purely two-dimensional reciprocal space approaches for modeling PCSELs include plane wave expansion (PWE), which assumes that the PC layer is extended infinitely in the vertical direction. However, in a PCSEL, only a relatively small fraction of the optical mode overlaps with the PC layer since the mode is vertically confined due to the waveguide structure, which contradicts this assumption [20]. To address this effect, effective refractive indices may be introduced, which can be approximated by certain weighting schemes, according to the vertical intensity distributions of the guided mode [21]. Certain methods, such as coupled-wave theory (CWT) [11,16] and guided mode expansion (GME) [22], where the latter is implemented in the well-known Legume library [23,24], formulate the electromagnetic field as a linear combination of guided modes. These can be factorized into a vertical profile, determined by the effective slab waveguide, and a planar wave with an in-plane propagation direction. These two methods differ, for instance, in their treatment of higher-order modes. GME expands fields as an arbitrary number of interacting guided modes [23], while CWT only considers fundamental waves with higher-order in-plane waves being handled perturbatively [11,25], as discussed in our previous work [26]. While CWT implementations reported in literature known to us only consider one vertical (waveguide) mode, we here utilize the capability of GME to include higher-order vertical modes, which also allows for describing the undesirable lasing with wide emission angles, that has frequently been observed for our UV-C PCSELs [27]. More generally, GME is capable of explaining the influence of higher-order vertical modes on band structures and losses which is potentially relevant for PCSELs in any material system or wavelength. Furthermore, the capability of incorporating higher-order lateral modes enables the simulation of higher-order resonances in PCSELs which has been demonstrated in Ref. [28] for a square PC lattice utilizing GME.

Incorporating finite-size effects is essential for the estimation of modal loss rates [29] since lateral outcoupling would not be present in systems treated as infinitely extended, and additionally, lateral confinement affects vertical outcoupling behavior as well. However, realistically large PCSEL areas may consist of millions of PC unit cells, such that three-dimensional finite-difference methods that require hundreds of discretization cells per unit cell [30] become prohibitively inefficient for such systems [29]. Therefore, modifications to CWT incorporating slowly varying envelopes have been investigated [16,29], which aim to express optical fields as a linear combination of plane waves with wavelengths matching lattice constants and spatially dependent slowly varying amplitudes. These are discretized on a substantially coarser grid, and thus, this method can be considered as a hybrid between real- and reciprocal-space approaches.

In Section 2, the underlying concepts behind GME are explained, and results for infinite structures are compared to CWT and angular-resolved photoluminescence measurements [21]. Moreover, a finite-area GME utilizing slowly varying envelopes is investigated in Section 3, which generalizes the existing approach based on CWT [16,29] insofar as higher-order lateral modes are incorporated as basis functions. Finally, in Section 4 the occurrence of the experimentally observed wide-angle lasing that is also predicted by GME simulations by considering higher-order waveguide modes is discussed.

2. Simulation approaches for infinite structures

2.1. Reciprocal space expansion models

Both CWT and GME aim to solve the stationary wave equation for nonmagnetic media given by Eq. (1),

$$\nabla \times \left(\frac{1}{\varepsilon_r(\mathbf{r})} \nabla \times \mathbf{H}(\mathbf{r}) \right) = \frac{\omega^2}{c^2} \mathbf{H}(\mathbf{r}), \tag{1}$$

assuming a stationary magnetic field $\hat{\mathbf{H}}(\mathbf{r}, t) = \mathbf{H}(\mathbf{r}) e^{i\omega t}$, where $\varepsilon_r(\mathbf{r})$ denotes the relative electric permittivity, c the speed of light in vacuum, and ω the angular eigenfrequency [22]. Within the photonic crystal layer, the dielectric permittivity is a periodic function, $\varepsilon_r(\mathbf{r}) = \varepsilon_r(\mathbf{r} + \mathbf{R})$, with

Optics EXPRESS

respect to all lattice vectors $\mathbf{R} = p\mathbf{a}_1 + q\mathbf{a}_2$ with primitive lattice vectors $\mathbf{a}_{1,2}$ and $p, q \in \mathbb{Z}$. These lattice vectors are illustrated in Fig. 1(a) for a two-dimensional hexagonal photonic crystal lattice.

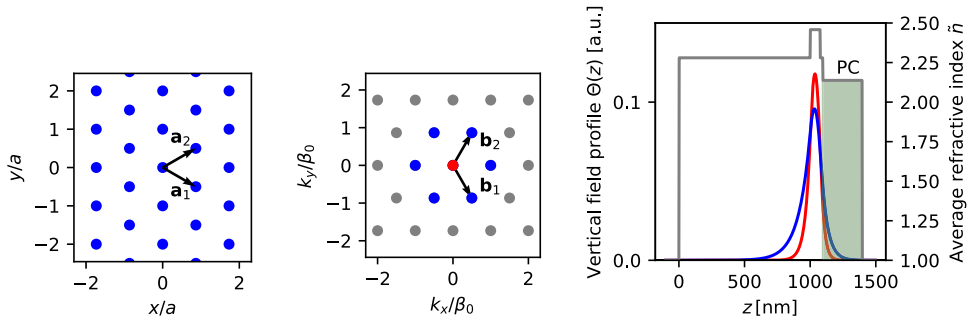

(a) (b) (c)

Fig. 1. (a) Hexagonal lattice in real-space. (b) Corresponding reciprocal lattice, with wavevectors for the six fundamental plane waves with magnitude β_0 (blue dots) and radiative (red dot) as well as higher-order waves (gray dots). (c) Refractive indices of effective slab waveguide $\tilde{n}$ (gray) and fundamental ($\gamma = 1$) vertical field profiles $\Theta(z)$ for first order reciprocal lattice vector with $|\mathbf{G}| = \beta_0$ (blue) and second order reciprocal lattice vector with $|\mathbf{G}| = \sqrt{3}\beta_0$ (red). The shaded area indicates the photonic crystal layer.

According to Bloch's theorem, stationary modes can be expressed in the form of Eq. (2),

$$\mathbf{H}(\mathbf{r}) = \sum_{\mathbf{G}} d_{\mathbf{G}}\, \mathbf{H}_{\mathbf{G}}(z) e^{i(\mathbf{G}+\mathbf{k})\cdot\mathbf{r}_\parallel}, \tag{2}$$

where $\mathbf{G} = m\mathbf{b}_1 + n\mathbf{b}_2$, $m, n \in \mathbb{Z}$ denote reciprocal lattice vectors with the primitive reciprocal vectors fulfilling $\mathbf{a}_i \cdot \mathbf{b}_j = 2\pi\delta_{i,j}$, as depicted in Fig. 1(b). The magnitude of the fundamental $\mathbf{G}$ is denoted by β_0 and $\mathbf{r}_\parallel$ indicates the lateral projection of the position vector. For each wavevector $\mathbf{k}$ in the first Brillouin zone, solving the eigenproblem yields a set of modes with coefficients $d_{\mathbf{G}}(\mathbf{k})$ and eigenfrequencies $\omega(\mathbf{k})$, thereby defining the photonic dispersion relation [11,31].

Analogous to several works regarding PCSEL simulations [10,11,16,32], electromagnetic fields are assumed to exhibit purely transversal electric (TE) polarization throughout this work, which is justified by the larger gain for TE in UV-C AlGaN quantum wells [33]. It has to be emphasized that this is an approximation, since solutions cannot be separated into pure TE and transversal magnetic (TM) fields in general, due to a missing horizontal mirror plane with respect to the dielectric permittivity [31]. However, the TM-dominated branches of the full band structure lie in a different wavelength range due to the strong birefringence of about 3% of AlN [34], such that the crossings of TE and TM modes occur outside the regions of interest. The electromagnetic field is therefore expanded in TE guided modes as indicated in Eq. (3),

$$\mathbf{H}(\mathbf{r}) = \sum_{\mathbf{G},\gamma} d_{\mathbf{G},\gamma} \mathbf{H}^{\text{guided}}_{\mathbf{G}+\mathbf{k},\gamma}(\mathbf{r}), \quad \mathbf{E}(\mathbf{r}) = \sum_{\mathbf{G},\gamma} c_{\mathbf{G},\gamma} \mathbf{E}^{\text{guided}}_{\mathbf{G}+\mathbf{k},\gamma}(\mathbf{r}), \tag{3}$$

where the electric field components of the guided modes can be expressed in the form given by Eq. (4),

$$\mathbf{E}^{\text{guided}}_{\mathbf{G}+\mathbf{k},\gamma} = (\rho_{\mathbf{G}+\mathbf{k}}\, \hat{e}_x + \eta_{\mathbf{G}+\mathbf{k}}\, \hat{e}_y)\, \Theta_{\mathbf{G}+\mathbf{k},\gamma}(z)\, e^{i(\mathbf{G}+\mathbf{k})\cdot\mathbf{r}_\parallel}. \tag{4}$$

For each wavevector $\mathbf{G}+\mathbf{k}$, a set of vertical field profiles $\Theta_{\mathbf{G}+\mathbf{k},\gamma}(z)$ can be determined (indexed by γ), by considering an effective vertical slab waveguide with laterally averaged permittivities

Optics EXPRESS

[16], which is illustrated in Fig. 1(c). Due to the transversality constraint $\mathbf{E}^{\text{guided}}_{\mathbf{G}+\mathbf{k}} \perp \mathbf{G}+\mathbf{k}$ [16], the field prefactors can be expressed for $\mathbf{G}+\mathbf{k} \neq \mathbf{0}$ w.l.o.g. by Eq. (5),

$$\rho_{\mathbf{G}+\mathbf{k}} = \frac{G_y + k_y}{|\mathbf{G}+\mathbf{k}|}, \quad \eta_{\mathbf{G}+\mathbf{k}} = -\frac{G_x + k_x}{|\mathbf{G}+\mathbf{k}|}. \tag{5}$$

The discrete set of guided modes for a given slab waveguide structure does not form a complete basis set, in general, since there is a continuum of modes above the light line, $c\,|\mathbf{G}+\mathbf{k}|<\omega$, with oscillating, non-evanescent tails leaking out of the structure [31]. These radiative modes, however, cannot be directly included in the discrete basis set, as they are not appropriately normalizable. In order to estimate vertical radiative losses, these modes are taken into account by CWT and GME utilizing perturbation theory [16,22].

2.2. Guided mode expansion formulation for infinite systems

While GME is capable of considering both TE and TM polarization as well as polarization mixing [23], the following discussion considers only TE polarization as mentioned above, and is based on Refs. [22,23]. The guided modes for reciprocal lattice vectors $\mathbf{G}$ utilized as basis functions in GME are stationary states in an effective slab waveguide, where the lateral dependence of the permittivity is neglected. Therefore, they are supposed to fulfill the relations given in Eq. (6),

$$\begin{aligned} \nabla \times \mathbf{H}^{\text{guided}}_{\mathbf{G}+\mathbf{k},\gamma} &= i\varepsilon_0 \tilde{n}^2(z)\, \Omega_{\mathbf{G}+\mathbf{k},\gamma}\, \mathbf{E}^{\text{guided}}_{\mathbf{G}+\mathbf{k},\gamma} \\ \nabla \times \mathbf{E}^{\text{guided}}_{\mathbf{G}+\mathbf{k},\gamma} &= -i\mu_0\, \Omega_{\mathbf{G}+\mathbf{k},\gamma}\, \mathbf{H}^{\text{guided}}_{\mathbf{G}+\mathbf{k},\gamma} \end{aligned} \tag{6}$$

with the eigenfrequency $\Omega_{\mathbf{G}+\mathbf{k},\gamma}$, which might differ from the eigenfrequencies ω of the PCSEL with laterally varying $\varepsilon_r(\mathbf{r})$ in general. $\tilde{n}(z)$ specifies the laterally averaged refractive index (root-mean-square) defined by $\tilde{n}^2(z) \equiv 1/A_C \int_{A_C} \mathrm{dxdy}\, \varepsilon_r(\mathbf{r})$, where A_C refers to the area of one unit cell, and $\Omega_{\mathbf{G}+\mathbf{k},\gamma}$ represents the eigenfrequency of the guided mode. Other averaging schemes for $\tilde{n}(z)$ are viable as well and would not change the results significantly [22], as using a truncated, discrete set of basis functions always leads to an overdetermined eigenproblem [35].

Inserting Eq. (3) into Eq. (1), multiplying by $\mathbf{H}^{\text{guided}*}_{\mathbf{G}'+\mathbf{k},\gamma'}$ and integrating over one unit cell C (i.e. over its area and from $-\infty$ to ∞ in z-direction) leads to Eq. (7):

$$\sum_{\mathbf{G},\gamma} d_{\mathbf{G},\gamma} \int_C \mathrm{d}^3\mathbf{r}\, \mathbf{H}^{\text{guided}*}_{\mathbf{G}'+\mathbf{k},\gamma'} \cdot \nabla \times \left(\frac{1}{\varepsilon_r(\mathbf{r})} \nabla \times \mathbf{H}^{\text{guided}}_{\mathbf{G}+\mathbf{k},\gamma}(\mathbf{r}) \right) = \frac{\omega^2}{c^2} \sum_{\mathbf{G},\gamma} d_{\mathbf{G},\gamma} \int_C \mathrm{d}^3\mathbf{r}\, \mathbf{H}^{\text{guided}*}_{\mathbf{G}'+\mathbf{k},\gamma'} \cdot \mathbf{H}^{\text{guided}}_{\mathbf{G}+\mathbf{k},\gamma} \tag{7}$$

Integrating by parts on the left-hand side and neglecting the resulting surface term (which vanishes under Bloch-periodic boundary conditions over the cell C), and assuming that the guided modes are orthonormal (as they are eigenmodes of the Hermitian eigenvalue problem in Eq. (6)) yields Eq. (8):

$$\sum_{\mathbf{G},\gamma} d_{\mathbf{G},\gamma} \int_C \mathrm{d}^3\mathbf{r}\, \frac{1}{\varepsilon_r(\mathbf{r})} \left(\nabla \times \mathbf{H}^{\text{guided}*}_{\mathbf{G}'+\mathbf{k},\gamma'} \right) \cdot \left(\nabla \times \mathbf{H}^{\text{guided}}_{\mathbf{G}+\mathbf{k},\gamma} \right) = \frac{\omega^2}{c^2} d_{\mathbf{G}',\gamma'}. \tag{8}$$

By rewriting the integral on the left-hand side as matrix element $L_{\mathbf{G}',\gamma',\mathbf{G},\gamma}$, one obtains the matrix-vector eigenvalue problem given by Eq. (9):

$$\sum_{\mathbf{G},\gamma} L_{\mathbf{G}',\gamma',\mathbf{G},\gamma}\, d_{\mathbf{G},\gamma} = \frac{\omega^2}{c^2} d_{\mathbf{G}',\gamma'}. \tag{9}$$

This equation can be solved numerically using the explicit form of the matrix elements assuming TE polarization which is derived in Supplement 1 Section S1.

Optics EXPRESS

The above derivation does not yet consider coupling to radiative modes, so the eigenfrequencies ω do not contain information about vertical outcoupling (radiation loss) rates. Vertical outcoupling in the GME method is treated using perturbation theory, involving overlap of the eigenmode with the radiative modes of in-plane wavevector $\mathbf{k}$ and frequency ω. The imaginary part of the complex-valued frequency ω' can be computed by Eq. (10) according to Fermi's Golden Rule [23]:

$$\Im\mathrm{m}(\omega'^2) = -\pi c^2 \sum_{\sigma} |P(\mathbf{k}, \omega, \sigma)|^2 \rho(\mathbf{k}, \omega). \tag{10}$$

Above sum considers both polarizations of the radiative mode, indexed by σ, and $P(\mathbf{k}, \omega, \sigma)$ denotes the interaction integral between the solution and the radiative mode for $\mathbf{k}, \omega$ that is given by Eq. (11):

$$P(\mathbf{k}, \omega, \sigma) = \sum_{G,\gamma} d^*_{\mathbf{G},\gamma} \int_C \mathrm{d}\mathbf{r}^3 \, \mathbf{H}^{\mathrm{guided}*}_{\mathbf{G}+\mathbf{k},\gamma} \cdot \nabla \times \left(\frac{1}{\varepsilon_r(\mathbf{r})} \nabla \times \mathbf{H}^{\mathrm{rad}}_{\sigma}(\mathbf{k}, \omega) \right). \tag{11}$$

$\mathbf{H}^{\mathrm{rad}}_{\sigma}(\mathbf{k}, \omega)$ represents the radiative mode of polarization σ. The density of states of radiative modes, $\rho(\mathbf{k}, \omega)$, including both upward and downward radiation directions, is given by Eq. (12),

$$\rho(\mathbf{k}, \omega) = \frac{\sqrt{\varepsilon_{r,o}}}{2\pi} \frac{1}{\sqrt{\omega^2/c^2 - k^2/\varepsilon_{r,o}}}, \tag{12}$$

where $\varepsilon_{r,o}$ indicates the permittivities above and below the epitaxial structure [23], which are both assumed to be 1 corresponding to air layers, such that only one common light cone has to be considered. Furthermore, it is assumed that $(\mathbf{k}, \omega)$ lies within the light cone, i.e. $\omega > c|\mathbf{k}|$, and all scattered wavevectors $\mathbf{k} + \mathbf{G}$ are outside the light cone such that they do not have to be taken into account in Eq. (10) unlike Ref. [23]. The vertical decay rates of the intensities are obtained by $1/\tau = 2\Im\mathrm{m}(\omega')$, where the factor of two takes the relationship between the field amplitudes and intensities into account.

2.3. Results for infinite devices

To demonstrate the GME approach for laterally (in-plane) infinite PCSEL structures, we compute photonic band structures for an UV-C PCSEL based on a hexagonal lattice with one circular air hole in its unit cell, as illustrated in Fig. 1(a). This hexagonal lattice geometry has been demonstrated experimentally in our previous studies [7], as it is expected to enable superior 2D feedback compared to square lattices. This results from the greater number of in-plane scattering directions in the former. Additionally, fundamental waves propagating in orthogonal directions do not couple in a square lattice for TE polarization [10,36]. The circular holes lead to very low vertical outcoupling (that is even entirely forbidden due to symmetry in infinite PCSELs [29]) which lowers the overall thresholds, which is important in first device demonstrations. In finite-sized PCSELs, as real devices are, the small vertical outcoupling at $\mathbf{k} \neq \mathbf{0}$ leads to doughnut-shaped far-fields [7,16,37]. However, the methods presented in this work should be applicable to arbitrary hole shapes and lattice types.

Figure 2 depicts the photonic band structure measured by angular resolved photoluminescence and simulated by both CWT (solid black lines) and GME (solid white lines) for infinitely extended PCSELs assuming the epitaxial structure given in Table 1, a lattice constant $a = 137$ nm, and a hole fill factor of $FF = 15\%$. Furthermore, simulations assume that the structure is surrounded by infinitely extended air layers with refractive index of $n = 1$, instead of taking the sapphire substrate into account. This approximation is justified by the significant change in refractive index at the substrate-cladding interface, such that evanescent tails are decaying rapidly towards the substrate. An additional validation is provided in Section S2 of the Supplement 1. Only the fundamental

Optics EXPRESS

vertical (waveguide) mode with $\gamma = 1$ has been taken into account in these simulations, whereas higher-order vertical modes have been neglected to enable a direct comparison with CWT, which in our implementation considers a single vertical mode. For the GME method, a basis set including $N_{\mathbf{G}} = 42 + 1$ reciprocal lattice vectors (i.e. 42 guided modes, plus one mode for $\mathbf{G} = \mathbf{0}$ representing the radiative field) have been taken into account which yield reasonably converged solutions. Opposed to that, the CWT simulation only considers basis sets of $N_{\mathbf{G}} = 6$ fundamental waves [25] and treats higher-order waves as a perturbation [16]. Observed discrepancies between CWT and GME (black and white lines, respectively) are essentially attributed to the different treatment of higher-order lateral modes [26], and to the fact that CWT considers the Fourier expansion of the dielectric constant $\varepsilon(\mathbf{r})$, whereas GME incorporates the Fourier expansion of $\varepsilon^{-1}(\mathbf{r})$ [22], which potentially changes the convergence behavior [38,39]. Comparisons of the simulated band structures with the results from angular resolved photoluminescence (PL) spectroscopy reveal better agreements for CWT than GME. The latter predicts too large band gaps at the Γ point as well as too small curvatures of the bands, suggesting that coupling effects are eventually overestimated. Studies with systematic variations of $N_{\mathbf{G}}$ presented in Section S3 of the Supplement 1 suggest that the band splitting increases with $N_{\mathbf{G}}$.

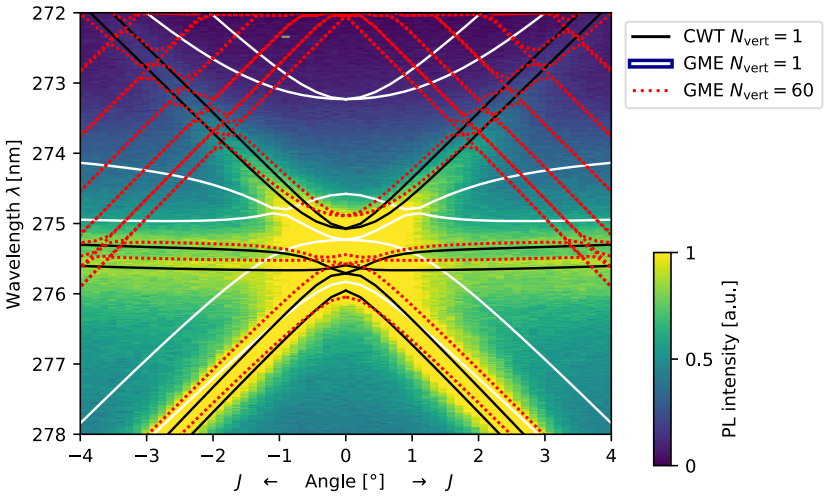

Fig. 2. Angular resolved photoluminescence spectrum of a UV-C-PCSEL along the Γ – J direction with fill factor $FF = 15\%$ and lattice constant $a = 137$ nm, optically pumped below threshold (color-coded background). Black curves show the CWT band structure, and solid white curves show the GME band structure including only the fundamental vertical (waveguide) mode assuming an infinite PC. Dotted red lines indicate band structures obtained by GME incorporating the first $N_{\text{vert}} = 60$ vertical modes.

Table 1. Assumed thicknesses and refractive indices *n* of the vertical epitaxial structure, which are considered in the simulations [26]. For the PC layer, the averaged refractive index for *FF* = 15% has been specified

Layer	Material	Thickness [nm]	n
PC	AlN / Air	300	2.137
Upper cladding	AlN	20	2.280
Core + QWs	$Al_{0.7}Ga_{0.3}N$	76	2.458
Lower cladding	AlN	1730	2.280

Optics EXPRESS

The red dotted lines in Fig. 2 denote the band structures obtained with GME using $N_{\text{vert}} = 60$ vertical (waveguide) modes, rather than only the fundamental one. In total, $N_{\mathbf{G}} \times N_{\text{vert}} = (42 + 1) \times (60)$ guided modes are considered, one for each γ and $\mathbf{G}$. The resulting band splitting is markedly smaller than that of the GME calculation with only the fundamental mode and is in close agreement with both the CWT results and the experimental data. Interaction with the large number of cladding modes originating from the thick lower cladding layer reduces the band splitting, thereby counteracting the effects of higher-order lateral modes. Systematic studies with varying N_{vert} are presented in the Supplement 1 Section S3. In conclusion, the CWT delivers satisfactory results for our epitaxial structure, even though it omits higher-order vertical modes and treats lateral modes perturbatively. While the GME with an expanded basis set requires more computational effort (while it can still be performed on an average personal computer within a few minutes), we argue that it constitutes a more general approach.

As neither CWT nor GME is a rigorous approach due to the incompleteness of their set of guided modes [40], we conducted Rigorously Coupled Wave Theory (RCWA) [41] simulations for the same structure which is a first-principles method. A direct comparison which is presented in Section S3 of the Supplement 1 reveals excellent agreement between RCWA and GME which demonstrates the accuracy of GME for our structures.

Moreover, the GME predicts avoided crossings at interaction points with emerging cladding mode bands (additional red lines in Fig. 2), enabling low-threshold states that cannot be captured by conventional CWT formulations; these phenomena will be examined in Section 4.

For all simulations shown in Fig. 2, intrinsic material dispersion effects are taken into account, which was necessary in order to obtain similar slopes of the bands compared to the experiment. Details regarding the estimation of influences from material dispersion are presented in Supplement 1 Section S4. Furthermore, the etched PC structure might exhibit non-vertical side walls, contrary to the cylindrical holes assumed in the simulations, which might explain any remaining discrepancies between the numerical simulations and experimental data.

3. Finite-area guided mode expansion

3.1. Formulation

The efficient modeling of finite-sized devices based on CWT, obviating the need to discretize the entire PCSEL with finite elements, has been demonstrated in Refs. [16,29]. In this section, a finite-area method based on GME will be implemented, which generalizes the slowly varying envelope approach based on CWT to a basis set including an arbitrary number of guided modes. This approach can be similarly considered as a multi-scale model [42,43], as it incorporates both microscopic properties on the wavelength scale, and their modulation on the larger length scale of the entire device.

In the finite-area GME approach the electric field is expanded in a basis of guided modes with position dependent coefficients, $c_{\mathbf{G},\gamma}(x, y)$, in the form of Eq. (13):

$$\mathbf{E}(\mathbf{r}) = \sum_{\mathbf{G},\gamma} c_{\mathbf{G},\gamma}(x, y)\,(\rho_{\mathbf{G}}\,\hat{e}_x + \eta_{\mathbf{G}}\,\hat{e}_y)\,\Theta_{\mathbf{G},\gamma}(z) e^{i\mathbf{G}\cdot\mathbf{r}_\parallel}. \tag{13}$$

While this expansion is similar to existing finite-area CWT implementations utilizing slowly varying envelopes [16,29], the proposed method differs from those, as the expansion includes an arbitrary number of reciprocal lattice vectors $\mathbf{G}$, as well as potentially greater sets of vertical modes, indexed by γ.

For the derivation of the finite-area GME method, we consider Eq. (14):

$$\frac{1}{\varepsilon_r(\mathbf{r})}\nabla \times \nabla \times \mathbf{E}(\mathbf{r}) = \frac{\omega^2}{c^2}\mathbf{E}(\mathbf{r}). \tag{14}$$

Optics EXPRESS

In contrast to Eq. (1), the operator appearing on the left-hand side is non-Hermitian with respect to the standard inner product $\langle \mathbf{E}_1, \mathbf{E}_2 \rangle = \int \mathrm{d}^3\mathbf{r}\, \mathbf{E}_1^* \cdot \mathbf{E}_2$ [35]. Since GME necessarily employs an incomplete basis set [22], we do not anticipate this non-Hermiticity to introduce substantial inaccuracies. Moreover, we demonstrate in the Supplement 1 (Section S5) that our finite-area GME implementation is capable of accurately reproducing nearly identical band structures to those obtained with the regular infinite GME model. By inserting the expansion of the electric field in Eq. (13) and the Fourier series for the inverse electric permittivity $\varepsilon_r^{-1}(\mathbf{r}) = \sum_{\tilde{\mathbf{G}}} S_{\tilde{\mathbf{G}}}(z)\, e^{i\tilde{\mathbf{G}}\cdot\mathbf{r}_\parallel}$ into Eq. (14), one obtains Eq. (15),

$$\begin{aligned}\frac{1}{\varepsilon_r(\mathbf{r})}\nabla\times\nabla\times\mathbf{E}(\mathbf{r}) &\simeq -\sum_{\tilde{\mathbf{G}},\mathbf{G}',\gamma} S_{\tilde{\mathbf{G}}}(z) e^{i\tilde{\mathbf{G}}\cdot\mathbf{r}_\parallel}\nabla^2\left(c_{\mathbf{G}',\gamma}(x,y)\,\mathbf{E}^{\text{guided}}_{\mathbf{G}',\gamma}(\mathbf{r})\right)\\ &\simeq \sum_{\tilde{\mathbf{G}},\mathbf{G}',\gamma} S_{\tilde{\mathbf{G}}}(z)\, e^{i(\tilde{\mathbf{G}}+\mathbf{G}')\cdot\mathbf{r}_\parallel}(\eta_{\mathbf{G}'}\,\hat{e}_x + \rho_{\mathbf{G}'}\,\hat{e}_y)\\ &\cdot\left(\left[|\mathbf{G}'|^2 - \frac{\partial^2}{\partial z^2}\right]\Theta_{\mathbf{G}',\gamma}(z) - 2i\Theta_{\mathbf{G}',\gamma}(z)\mathbf{G}'\cdot\nabla\right)c_{\mathbf{G}',\gamma}(x,y)\\ &= \frac{\omega^2}{c^2}\sum_{\mathbf{G},\gamma} c_{\mathbf{G},\gamma}(x,y)\, e^{i\mathbf{G}\cdot\mathbf{r}_\parallel}\,\Theta_{\mathbf{G},\gamma}(z)\,(\eta_{\mathbf{G}}\,\hat{e}_x + \rho_{\mathbf{G}}\,\hat{e}_y).\end{aligned} \tag{15}$$

In the first step, the assumption that the slowly varying envelope does not introduce significant TM contributions, was utilized, such that $\nabla\cdot\mathbf{E}(\mathbf{r}) = 0$ and hence $\nabla\times\nabla\times\mathbf{E}(\mathbf{r}) = -\nabla^2\mathbf{E}(\mathbf{r})$ holds. Moreover, second derivatives of the envelopes have been neglected similar to the CWT formulation [29], which is justified by the assumption, that the envelope is much more slowly varying than the in-plane wavefunctions, i.e. $|\nabla_{x,y} c_{\mathbf{G},\gamma}/c_{\mathbf{G},\gamma}| \ll |\mathbf{G}|$.

The vertical profiles $\Theta_{\mathbf{G},\gamma}(z)$ are assumed to obey Eq. (16) arising from the effective slab waveguide,

$$\left(|\mathbf{G}|^2 - \frac{\partial^2}{\partial z^2}\right)\Theta_{\mathbf{G},\gamma}(z) = \tilde{n}^2(z)\frac{\Omega^2_{\mathbf{G},\gamma}}{c^2}\Theta_{\mathbf{G},\gamma}(z), \tag{16}$$

which is inserted into the above equation. Relabeling $\mathbf{G} = \tilde{\mathbf{G}} + \mathbf{G}'$, and noting that above equality has to hold for every prefactor of the exponentials individually, leads to Eq. (17):

$$\begin{aligned}\sum_{\mathbf{G}',\gamma} S_{\mathbf{G}-\mathbf{G}'}(z)\,\Theta_{\mathbf{G}',\gamma}(z)\left(\tilde{n}^2(z)\frac{\Omega^2_{\mathbf{G}',\gamma}}{c^2} - 2i\mathbf{G}'\cdot\nabla\right)c_{\mathbf{G}',\gamma}(x,y)\,(\eta_{\mathbf{G}'}\,\hat{e}_x + \rho_{\mathbf{G}'}\,\hat{e}_y)\\ = \frac{\omega^2}{c^2}\sum_{\gamma}\Theta_{\mathbf{G},\gamma}(z)\,c_{\mathbf{G},\gamma}(x,y)\,(\eta_{\mathbf{G}}\,\hat{e}_x + \rho_{\mathbf{G}}\,\hat{e}_y).\end{aligned} \tag{17}$$

Both sides are multiplied by $[\eta_{\mathbf{G}}, \rho_{\mathbf{G}}, 0]^T\,\Theta^*_{\mathbf{G},\tilde{\gamma}}(z)\,\tilde{n}^2(z)$, in analogy to the GME formulation for infinite systems, and integrated over z, which results in Eq. (18):

$$\begin{aligned}&\sum_{\mathbf{G}',\gamma}(\eta_{\mathbf{G}}\eta_{\mathbf{G}'} + \rho_{\mathbf{G}}\rho_{\mathbf{G}'})\\ &\cdot\int_{-\infty}^{\infty}\mathrm{d}z\, S_{\mathbf{G}-\mathbf{G}'}(z)\,\Theta^*_{\mathbf{G},\tilde{\gamma}}(z)\,\Theta_{\mathbf{G}',\gamma}(z)\,\tilde{n}^2(z)\left(\tilde{n}^2(z)\frac{\Omega^2_{\mathbf{G}',\gamma}}{c^2} - 2i\mathbf{G}'\cdot\nabla\right)c_{\mathbf{G}',\gamma}(x,y)\\ &= \frac{\omega^2}{c^2}\sum_{\gamma}\int_{-\infty}^{\infty}\mathrm{d}z\,\Theta^*_{\mathbf{G},\tilde{\gamma}}(z)\,\Theta_{\mathbf{G},\gamma}(z)\,\tilde{n}^2(z)\,c_{\mathbf{G},\gamma}(x,y).\end{aligned} \tag{18}$$

Introducing matrices C and F, covering above integral and certain prefactors on the left hand side, as well as matrix J covering the integral on the right hand side, allows one to formulate the

Optics EXPRESS

above equation in the form of Eq. (19):

$$\sum_{\mathbf{G}',\gamma} \left(C_{\mathbf{G},\tilde{\gamma},\mathbf{G}',\gamma} - 2iF_{\mathbf{G},\tilde{\gamma},\mathbf{G}',\gamma}\mathbf{G}' \cdot \nabla \right) c_{\mathbf{G}',\gamma}(x,y) = \frac{\omega^2}{c^2} \sum_{\gamma} J_{\tilde{\gamma},\gamma} c_{\mathbf{G},\gamma}(x,y). \tag{19}$$

The coefficients $c_{\mathbf{G},\gamma}(x,y)$ are discretized on an artificial grid, which will be discussed in more detail in the following section. The coefficients at each position for every considered reciprocal lattice vector $\mathbf{G}$ and vertical mode γ form the unknown variables in an eigenvalue problem. The term in Eq. (19) involving the gradient will be estimated by a finite difference between coefficients of neighboring positions, which introduces spatial coupling of those coefficients, besides the coupling between waves with different $\mathbf{G}$, mediated by the PC lattice. Due to the slowly varying nature of the envelope function, the spatial discretization can be performed on an artificial grid with lattice constants much greater than those of the PC lattice. This allows for a much more efficient computation compared to a FDTD simulation, as the latter would deal with many variables per PC unit cell.

In this work, we focus on laterally homogeneous PCs. In principle, this framework can be generalized to handle certain laterally varying structural paramaters such as fill factors by utilizing position dependent coupling matrices. However, it has to be noted that systems with spatially varying lattice constants cannot be modeled without major modifications, as this would introduce different fundamental reciprocal lattice vectors which contradicts the assumption from Eq. (19). Geometrical aspects of the discretization and locations for stored variables are discussed in more detail in the following section.

3.2. Results for circular finite-sized devices

For the analysis of finite-sized PCSELs and the emerging finite-size effects, we focus on PCSELs with circular PC areas in this work, whereas a generalization of this method to different shapes should be straightforward. In this section, we present stationary states in such devices, obtained by the finite-area GME method. For simplicity and compatibility with the finite-sized CWT approach, only the fundamental vertical guided mode is taken into account with $\gamma = 1$ in the GME calculations, such that this index is thus omitted in the following. However, higher-order vertical modes severely affect band structures obtained by GME as observed in Fig. 2, but we neglect this effect in this section, due to the resulting elevated computational requirements and focus on the effects emerging from higher-order *lateral* modes at first. The finite-area GME methodology will be demonstrated for multiple *vertical* modes in Section 4.2.

In order to realize transparent boundary conditions (i.e. outcoupling without reflections and no incoupling at the boundary), a staggered grid approach is employed [16,32]. This is accomplished by the use of a discretization grid, as illustrated in Fig. 3(b), where coefficients $c_{\mathbf{G}}(x,y)$ of fundamental wavevectors, illustrated by black arrows in Fig. 3, are stored as eigenvector elements for the midpoints of cell interfaces represented by orange dots.

Coefficients at the boundary in real space for fundamental wavevectors pointing inward are fixed to zero since those represent inward-propagating waves. Furthermore, it is assumed that the values of $c_{\mathbf{G}}(x,y)$ and their derivatives entering Eq. (19) are evaluated at the discretization cell centers. This is accomplished by averaging the two amplitudes for the same $\mathbf{G}$, stored at opposite cell interfaces. The directional derivatives $\mathbf{G} \cdot \nabla$ are evaluated at the cell centers as well by considering the finite-difference quotient between values at opposite cell interfaces for fundamental wavevectors.

An additional challenge compared to the finite-area CWT approach arises from the fact that not all wave vectors $\mathbf{G}$ point in the direction of neighboring cell centers, which is only valid for the fundamental wavevectors. Thus, the term involving the derivative in the direction of the wave vectors, $\mathbf{G} \cdot \nabla$, cannot always be directly evaluated, by considering only differences of $c_{\mathbf{G}}$ between neighboring cell centers. To circumvent this problem, all derivatives of $c_{\mathbf{G}}$ for higher-order $\mathbf{G}$

Optics EXPRESS

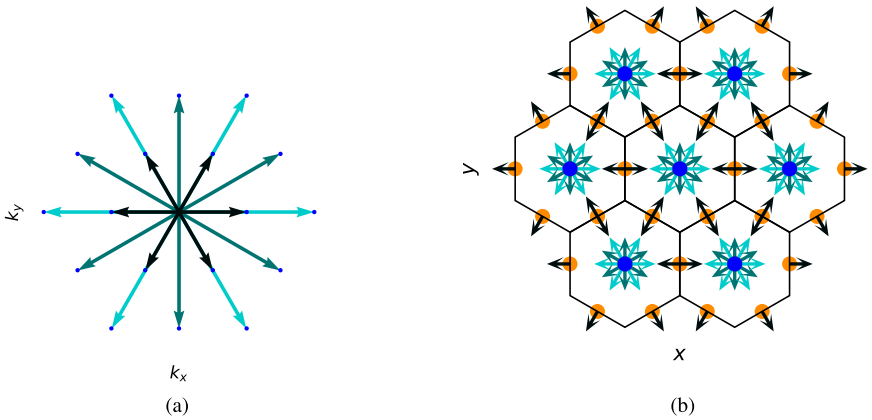

Fig. 3. (a) Representative set of reciprocal wavevectors taken into account for finite-area GME. (b) Discretization grid, where the cell centers are indicated by blue dots and the staggered positions at cell interfaces by orange dots. Only the coefficients for the first-order reciprocal wave vectors (black arrows) are stored as eigenvector entries at the staggered positions, whereas the coefficients for all higher-order wavevectors are stored at cell centers, and do not couple to neighboring cells.

are neglected, leaving only derivatives for fundamental $\mathbf{G}$ which is justified in Section S5 of the Supplement 1, such that storing them at staggered positions is not necessary. Instead, the coefficients of higher-order waves, represented by longer turquoise arrows in Fig. 3(a), are stored at cell centers, as illustrated in Fig. 3(b).

The imaginary part of the eigenvalue from Eq. (19) is assumed to represent only lateral loss rates, $\tau_{\mathrm{lat}}^{-1} = 2\Im\mathfrak{m}(\omega)$, as no coupling with the radiative field has been incorporated at this point. Therefore, vertical loss rates are calculated utilizing Fermi's Golden rule from Eq. (10), by decomposing the finite-sized mode into solutions of the infinite system with different wavevectors $\mathbf{k}$, where the detailed procedure is described in our previous paper [26]. The modal vertical loss rate is obtained by averaging the individual loss rates of the infinite solutions involved in this decomposition over reciprocal space, weighted by their intensity distribution.

The eigenmodes in a circular PCSEL with radius of $L = 100$ µm have been computed by finite-area GME for a discretization grid with $N_r = 8$ cells along the radius (for reference, Fig. 3(b) illustrates a lattice with $N_r = 1$). The resulting eigenspectra considering $N_{\mathbf{G}} = 6 + 1$ and $N_{\mathbf{G}} = 54 + 1$ guided modes are depicted in Fig. 4. For this moderately large PCSEL, the modal wavelengths of the solutions are approximately equal to the wavelengths of the infinite band structure at the Γ point (note that the infinite system wavelengths deviate from those shown in Fig. 2 as intrinsic material dispersion is neglected in Fig. 4). This suggests that effects from higher-order lateral modes are indeed taken into account by the finite-area GME implementation and that this particular approach to the staggered grid is appropriate. For each band, a finite-sized eigenstate with a compact intensity distribution and an intensity maximum in the center can be observed among the solutions with low total losses [16,29], as seen in Fig. 4(b) for the A mode, for example. Additionally, a so-called whispering gallery mode with a doughnut-shaped intensity distribution usually arises, referred to as W mode in the following, that has also been numerically [16] and experimentally [44] observed in literature. Remarkably, the modal wavelengths of the solutions for the finite device depend significantly on the lateral truncation order, suggesting that contributions from higher-order waves are relevant for finite-sized systems as well. Furthermore, the resulting wavelengths obtained by finite-area GME differ from those obtained by the finite-area CWT formulation, while discrepancies tend to increase for larger basis sets in finite-area GME,

Optics EXPRESS

which agrees with the observations for the wavelengths of infinite systems, as discussed in our previous work [26].

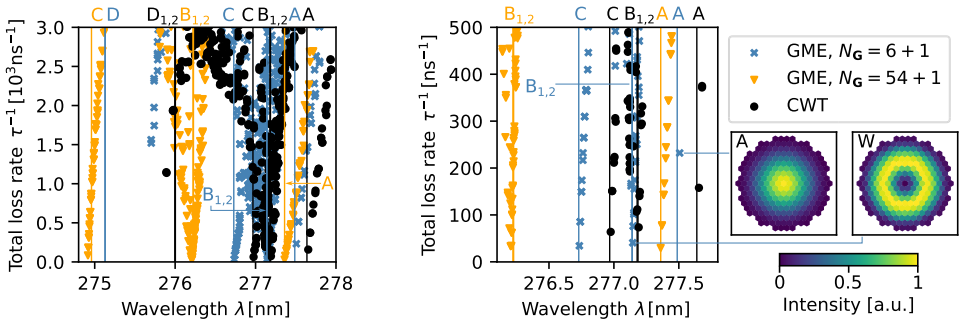

(a) (b)

Fig. 4. (a) Modal wavelengths and total loss rates of eigenmodes (subset) at the Γ point in a finite device with a radius of $L = 100$ μm, obtained using both, finite-area CWT and finite-area GME considering just the fundamental vertical mode. For the latter, two different numbers of guided modes, $N_\mathbf{G}$, have been considered. The symbols for the finite-sized D modes exceed the plotting region. (b) Zoomed-in version of (a), depicting the solutions with lowest loss rates. The spatial intensity distributions for the A and W mode obtained by finite-area GME are displayed, where blue lines point to the symbol for the corresponding solution. Vertical lines indicate the wavelengths of the infinite system in (a) and (b), calculated by the respective methods. Color-coded letters indicate the bands of the infinite system, labeled by A, B_1, B_2, C, D_1, and D_2.

Remarkably, discrepancies can be even observed between the finite-area CWT states and the finite-area GME simulation when considering only the fundamental lateral and vertical modes. We attribute this moderately small disagreement to the fact, that GME considers the expansion of $\varepsilon_r^{-1}(\mathbf{r})$ in the eigenvalue problem in the form of Eq. (1) while CWT considers the Fourier expansion of $\varepsilon_r(\mathbf{r})$, see Section S6 of the Supplement 1.

3.3. *Convergence properties of finite-area GME*

Figure 5 shows the dependence of the modal wavelengths and loss rates on the number of considered guided modes, obtained using finite-area GME for a circular system with radius $L = 100$ μm, where only the fundamental vertical mode has been considered.

The splitting between modal wavelengths tends to increase with $N_\mathbf{G}$, and convergence is observed for approximately $N_\mathbf{G} \geq 36$, corresponding to a truncation radius in reciprocal space of $G_{\max} \geq 3\beta_0$. This observation agrees with the convergence behavior of wavelengths in infinite systems at the Γ point reported in our previous work [26] and in Section S3 of the Supplement 1. Lateral loss rates of the A and B modes decrease substantially with increasing $N_\mathbf{G}$, which is interpreted as follows: a larger number of considered modes leads to stronger in-plane coupling effects and hence to increased backscattering, which reduces the rate at which the mode is laterally outcoupled through the device boundary.

Moreover, vertical losses of the D and C modes tend to increase with $N_\mathbf{G}$, which can be explained based on the larger number of modes coupling with the radiative field. In contrast to that, a decreasing vertical loss rate is reported for the A mode, which should not be overinterpreted, as this mode is dominated by lateral losses. The competing convergence behaviors of lateral and vertical losses lead to rather complex relationships between total loss rates and $N_\mathbf{G}$. Remarkably, considering different numbers of guided modes as basis functions might actually change the

Optics EXPRESS

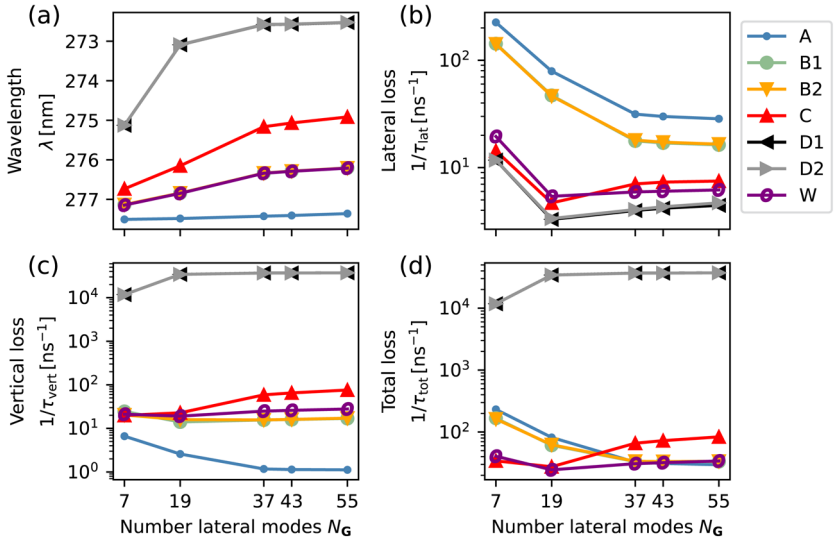

Fig. 5. (a) Modal wavelength, (b) lateral loss rates, (c) vertical loss rates, and (d) total loss rates as a function of the lateral truncation order, i.e. number of guided modes N_G, for a radius of $L = 100$ µm and a fill factor of $FF = 15\%$ calculated by finite-area GME considering only the fundamental vertical mode. The whispering gallery mode is denoted by W. Note that the curves for the D_1 and D_2 modes as well as the curves for the B_1 and B_2 modes overlap. In (a), the W mode overlaps with the B modes.

order of the loss rates, as seen in Fig. 5(d), and with that, the predicted lasing mode. Reasonably converged values of modal wavelengths and loss rates are reported for $N_\mathrm{G} \geq 36$, where the A and W modes exhibit the lowest total losses. Further studies might investigate the convergence behavior depending on the number of incorporated vertical modes.

4. Modeling of wide-angle lasing

4.1. Qualitative discussion

Many deep-UV PCSELs we have fabricated show the desired far-fields with narrow beam divergence. However, some PCSELs show in addition to the Γ point spot, lasing at a slightly lower wavelength producing bright spots in the far-field arranged in a hexagon [27] at angles of about 14.7° relative to the surface normal, as depicted in Fig. 6. The device has a radius of $L = 51.5$ µm and lattice constant of $a = 138$ nm. These high-angle lasing spots may be caused by coupling to higher-order vertical modes, which is discussed in the following.

All simulations presented above, except one in Fig. 2, employed only a single fundamental vertical field profile of the effective slab waveguide, as illustrated in Fig. 1(c). However, the relatively thick lower cladding layer allows many more modes as illustrated in Fig. 7(a), which can be obtained utilizing the transfer matrix method. For each vertical cladding mode, a band structure can be calculated by GME, which is illustrated in Fig. 7(b). The effective refractive index of the vertical modes decreases as the mode number increases. This causes a blueshift of the entire band structure with increasing mode number, as seen in Fig. 7(b). Moreover, the field overlap with the PC layer is affected, which leads to different coupling strengths and hence to different band curvatures as well as band splittings. Coupling effects between the individual band structures for different vertical modes are expected to arise at the intersection points, leading to avoided crossings where the bands split.

Optics EXPRESS

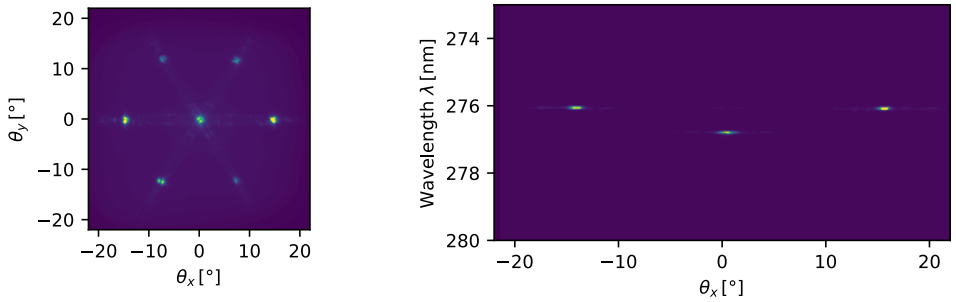

(a) (b)

Fig. 6. Emission characteristics of an optically pumped PCSEL with radius $L = 51.5$ µm and lattice constant $a = 138$ nm exhibiting wide-angle lasing. (a) Far-field and (b) angular resolved photoluminescence, both for pumping at twice the threshold.

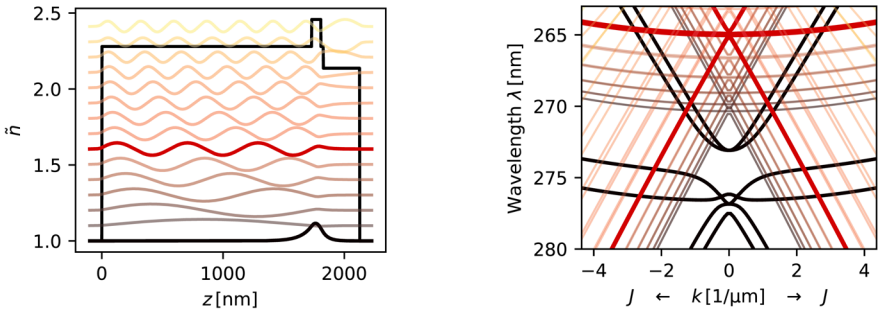

(a) (b)

Fig. 7. (a) Transversally averaged refractive index $\tilde{n}(z)$ (black solid profile, root-mean-square) and the first 15 vertical modes (color-coded curves), which have been vertically displaced for illustration purpose. (b) Resulting band structures with corresponding colors. At this point, no coupling between the vertical modes has been taken into account. For clarity, two vertical modes in (a) are highlighted that correspond to the two highlighted band structures in (b).

In order to investigate such interactions, GME simulations of the infinite system have been performed, which incorporate $N_{\text{vert}} = 60$ vertical and $N_{\mathbf{G}} = 42 + 1$ lateral modes simultaneously, also including the coupling effects between them. Red dotted curves in Fig. 8 visualize the resulting band structures for a lattice constant of $a = 137$ nm, together with the angle resolved PL spectrum (same as in Fig. 2 for a wider angle range). Notice, that the device parameters deviate slightly from those for the far-field shown in Fig. 6, for which no measured band structure was available. Additionally, material dispersion effects are considered, which are explained in Supplement 1 Section S4.

For each blueshifted band structure corresponding to higher-order vertical modes, the two bands with steep slopes (barely distinguishable for the depicted axis ranges) approach the rather shallow bands corresponding to the fundamental vertical mode. Instead of smooth intersections, avoided crossings emerge from coupling effects [45], as seen in Fig. 8(b) for certain bands.

The resulting curves include plateaus with close to vanishing slopes and hence zero group velocities, which lead to very low lateral loss rates. Eventually, the total losses of modes located at such plateaus become nearly as low as those of the modes located at the Γ point, such that lasing could occur at high angles. In particular, the locations of the broadest plateaus coincide

Optics EXPRESS

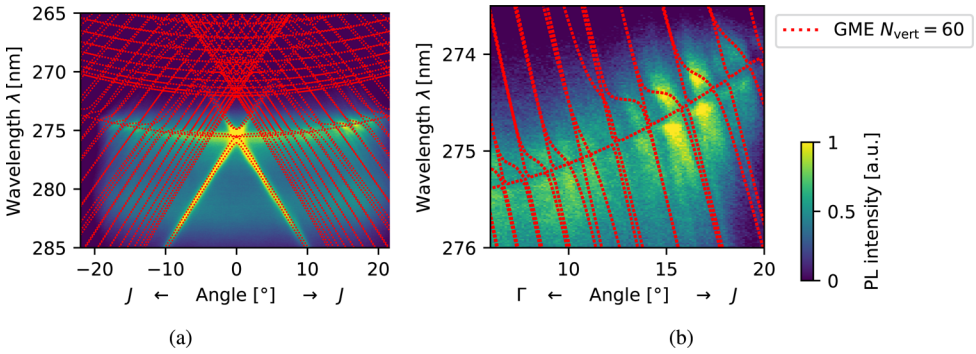

Fig. 8. (a) Angular resolved PL spectrum of a UV-C-PCSEL along the $\Gamma - J$ direction with fill factor $FF = 15\%$ and lattice constant $a = 137$ nm, optically pumped below threshold. Dotted red lines indicate band structures obtained by GME incorporating the first 60 waveguide modes. (b) Zoomed-in version of (a).

with the spots of highest intensities of the band structure measurement around 15° and 17°. These angles (the former in particular) are similar to the emission angles of ≈ 14.7° observed in Fig. 6, where discrepancies might be attributed to the fact that the presented far-field and band structure measurements were performed for distinct device parameters. In addition, device parameters of the real PCSEL might differ from the values assumed in the simulations. Furthermore, stripes with low intensities occur in between the avoided crossings in the angular resolved PL spectrum in Fig. 2, where the resulting coupled bands exhibit steeper slopes and thus high lateral losses. The short photon lifetime leads to very small emissions in those regions. Similar dark lines can also be observed in measured band structures that are reported in Refs [10,16,21]. In those works, structures with 1500 nm thick upper and lower claddings have been observed, such that interactions with cladding modes might have been the cause of those features in the band structures as well.

For any of the six directions equivalent to the $\Gamma - J$ direction, such avoided crossings with low threshold states emerge such that lasing might occur for six azimuthal angles, which agrees well with the approximate six-fold symmetry in the far-field in Fig. 6(a).

According to the angular resolved PL spectrum displayed in Fig. 6(b) along the $\Gamma - J$ direction above the threshold, the wavelengths of the wide-angle beams are shorter than the those of the vertical beam [27]. This agrees with the smaller wavelengths of the plateaus resulting from the GME simulation, relative to the Γ point modes. This observation also suggests, that the wide-angle beams probably arise indeed from dedicated lasing modes, instead of parasitic scattering effects, since the latter would preserve wavelengths, as observed in our earlier studies [7].

Which of the particular cladding modes enables the formation of wide-angle lasing modes is essentially determined by two criteria: First, the respective cladding mode is required to spatially overlap sufficiently with the active medium, allowing for elevated amplification. Second, its overlap with the fundamental vertical mode for $\gamma = 1$ within the PC layer must be large, which enhances coupling effects and thereby reduces the curvature of the arising avoided crossings, leading to lower group velocities and thus lower optical losses. Figure 9(a) shows the vertical overlap of cladding modes with the quantum well (QW) layers, $\Gamma_{\mathrm{QWs},\gamma} = \int_{\mathrm{QWs}} \mathrm{d}z\, |\Theta_{\mathbf{G},\gamma}|^2$. Our structure comprises three 2 nm thick QW layers separated by 5 nm thick $Al_{0.7}Ga_{0.3}N$ barrier layers in the center of the core layer. Additionally, the vertical overlaps with the fundamental mode within the PC layer, $\Gamma_{\mathrm{fund},\gamma} = \int_{\mathrm{PC}} \mathrm{d}z\, \Theta^*_{\mathbf{G},1} \Theta_{\mathbf{G},\gamma}$, are depicted. Note that the integration

Optics EXPRESS

region only involves the PC layer for the latter quantity, as only this region gives rise to coupling effects between different wavevectors.

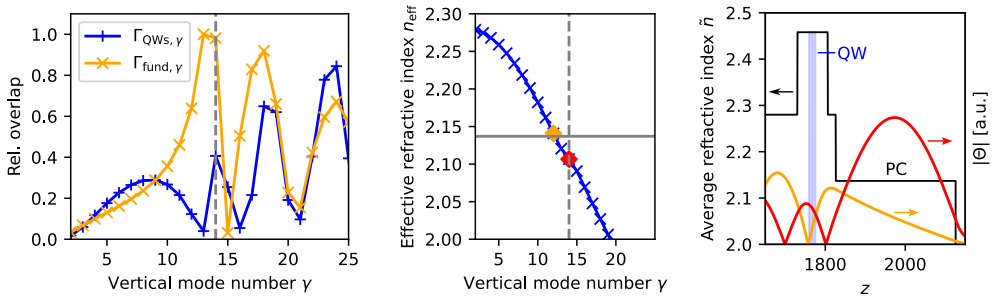

(a) (b) (c)

Fig. 9. (a) Vertical overlap of cladding modes with the quantum well (QW) layers (blue) and with fundamental vertical mode ($\gamma = 1$) within PC layer (orange). (b) Effective refractive index (neglecting intrinsic material dispersion) of vertical modes. The horizontal grey line indicates the averaged index $\tilde{n}$ in the PC layer. The vertical grey dashed line indicates $\gamma = 14$ in (a) and (b). (c) Absolute value, $|\Theta|$, of the mode for $\gamma = 12$ (orange) and $\gamma = 14$ (red). The QWs are indicated by the blue shaded region.

A monotonically increasing $\Gamma_{\text{fund},\gamma}$ is observed for $\gamma \leq 13$, where for $\gamma = 13$ and $\gamma = 14$, particularly large values arise. This results from the fact, that the effective refractive index of the modes, n_{eff}, as displayed in Fig. 9(b) is lower than the averaged index of refraction, $\tilde{n}$, of the PC layer for the first time for $\gamma = 13$. Consequently, the field tails exhibit exponentially decaying behavior for $\gamma<13$ with $n_{\text{eff}}>\tilde{n}$ in this region, while oscillatory behavior occurs for $\gamma \geq 13$ with $n_{\text{eff}}<\tilde{n}$, as seen in Fig. 9(c). For $\gamma = 13$ and $\gamma = 14$, where n_{eff} is just barely lower than $\tilde{n}$, the largest $\Gamma_{\text{fund},\gamma}$ are observed, whose values tend to oscillate with even larger γ. Remarkably, the overlap with the QW layers, $\Gamma_{\text{QWs},\gamma}$ simultaneously exhibits a local maximum for $\gamma = 14$ (dashed line in the figure), which coincides with the brightest spots in the vicinity of the corresponding avoided crossing in Fig. 8. In contrast to that, the profiles for $\gamma = 12$ and $\gamma = 13$ exhibit nodes near the QW layer (blue shaded regions in Fig. 9(c)) leading to small overlap.

4.2. *Finite-area GME with cladding modes*

To approximate the loss rates of the wide-angle lasing modes, and thus understand which are likely to lase or not, finite-area GME simulations are required since those are capable of including coupling effects between fundamental and higher-order vertical modes. This is accomplished by considering additional higher-order vertical modes with $\gamma>1$ in the formalism presented in Section 3.1. In contrast to the ordinary finite-area modes located at the Γ point, the modes giving rise to wide-angle lasing are assumed to exhibit non-vanishing wavevectors $\mathbf{k}$. Therefore, such eigenstates are expected to involve spatial modulations of the form $e^{i\mathbf{k}\cdot\mathbf{r}_\parallel}$, which would have to be adopted by the envelope functions $c_{\mathbf{G},\gamma}(x, y)$.

Unfortunately, the maximum wavevector $\mathbf{k}$ for those modulations is limited by the spatial Nyquist frequency resulting from the lattice constant of the discretization lattice, so that low-threshold modes with large k are eventually not accessible. To circumvent this limitation, the expansion of the electric field in Eq. (13) is modified by replacing the exponential term $e^{i\mathbf{G}\cdot\mathbf{r}_\parallel}$ by $e^{i(\mathbf{G}+\Delta\mathbf{k})\cdot\mathbf{r}_\parallel}$, where the wavevector $\Delta\mathbf{k}$ is supposed to approximately represent the region in reciprocal space, where the low-threshold modes are expected. This way, the envelope functions $c_{\mathbf{G},\gamma}(x, y)$ have to adopt slower oscillations with wavevector $\mathbf{k} - \Delta\mathbf{k}$. For this transformation, the values for the guided mode frequencies $\Omega_{\mathbf{G},\gamma}$, the vertical profiles $\Theta_{\mathbf{G},\gamma}$, the polarization

Optics EXPRESS

directions $\rho_{\mathbf{G}}, \eta_{\mathbf{G}}$, as well as the wavevectors themselves, must be changed in the matrix elements by replacing $\mathbf{G} \rightarrow \mathbf{G} + \Delta\mathbf{k}$ in Eq. (18).

In order to keep computational costs reasonable, we only consider the six fundamental lateral modes as well as the first 20 vertical modes in the following calculations which should be sufficient to investigate the the avoided crossing with vertical modes with strong overlap with the QWs and the fundamental vertical mode inside the PC. We consider a circular structure with a grid resolution with $N_r = 5$ cells along the radius. Simulations with larger N_{vert}, $N_{\mathbf{G}}$, and N_r which are presented in Supplement 1 Section S7 lead to nearly identical observations. The arising band structure of the infinite system assuming these vertical modes is depicted in Fig. 10(a) which exhibits several avoided crossings in the highlighted region that are clearly visible in the zoom-in in the left panel of Fig. 10(b). For our finite-area GME simulation, the parameter $\Delta\mathbf{k}$ is chosen to $6.45\ \mu\text{m}^{-1}\hat{e}_y$ (i.e. on the $\Gamma - J$ axis). This parameter has been chosen based on the location in k-space of the particular avoided crossing of interest with the vertical mode for $\gamma = 14$. This wavevector also agrees well with the angle of $\approx 16.5^\circ$ where one of the bright spots is observed in the PL measurement in Fig. 8(b). Additional simulations with varying $\Delta\mathbf{k}$ which are presented in Section S7 of the Supplement 1 also strengthen this choice. The wavelengths and total loss rates for a circular PCSEL with radius $L = 25\ \mu\text{m}$, obtained by finite-area GME assuming these parameters and vertical modes, are depicted in the right panel of Fig. 10(b). Notably, solutions with wavelengths coinciding with those of the bands labeled R and S of the infinite system at $\Delta k_y = 6.45\ \mu\text{m}^{-1}$ exhibit relatively low total losses. This observation agrees with the small slopes of the corresponding bands of the infinite system, which lead to low group velocities and thereby low (lateral) loss rates as observed in the left panel of Fig. 10(b) and for the R (red) and S (green) bands in Fig. 10(c). Among these two branches, the lowest loss rates arise for certain finite-area solutions corresponding to the S band, potentially enabling wide-angle lasing. In contrast to that, elevated vertical loss rates, which are color-coded in Fig. 10(b), as well as larger slopes enhance total loss rates of solutions corresponding to the R band. Therefore, the corresponding lowest threshold gains of the S band might enable stationary coherent oscillations due to the vanishing group velocities in the vicinity of the saddle-like point as seen in Fig. 10(c). On the other hand, no solutions with low (lateral) losses arise with wavelengths corresponding to the remaining bands due to their larger slopes and thus elevated group velocities.

In Section S7 of the Supplement 1, we provide evidence that the resulting eigenspectrum of the finite-area GME simulation is robust against reasonable changes in the parameter Δk, as emerging oscillations in the envelopes $c_{\mathbf{G},\gamma}(x, y)$ allow compensation for wavevector detuning. The existence of additional low-threshold states at the adjacent avoided crossings is reported and discussed in that section as well. To assess the robustness of the finite-area GME simulations, we conducted additional runs with larger numbers of vertical and lateral modes as well as grid resolutions. As the results of these runs, which are presented in Section S7 of the Supplement 1, are relatively insensitive to these parameters, we conclude that the overall findings are reasonably robust. However, it has to be emphasized that the underlying finite-area GME model is not a first-principles method and that the quantitative correctness of the loss rates cannot be rigorously validated. To allow a more realistic description of the wide-angle lasing, further simulations could also include intrinsic absorptions and gain, which might also vary laterally due to inhomogenities in the pumping spot.

Optics EXPRESS

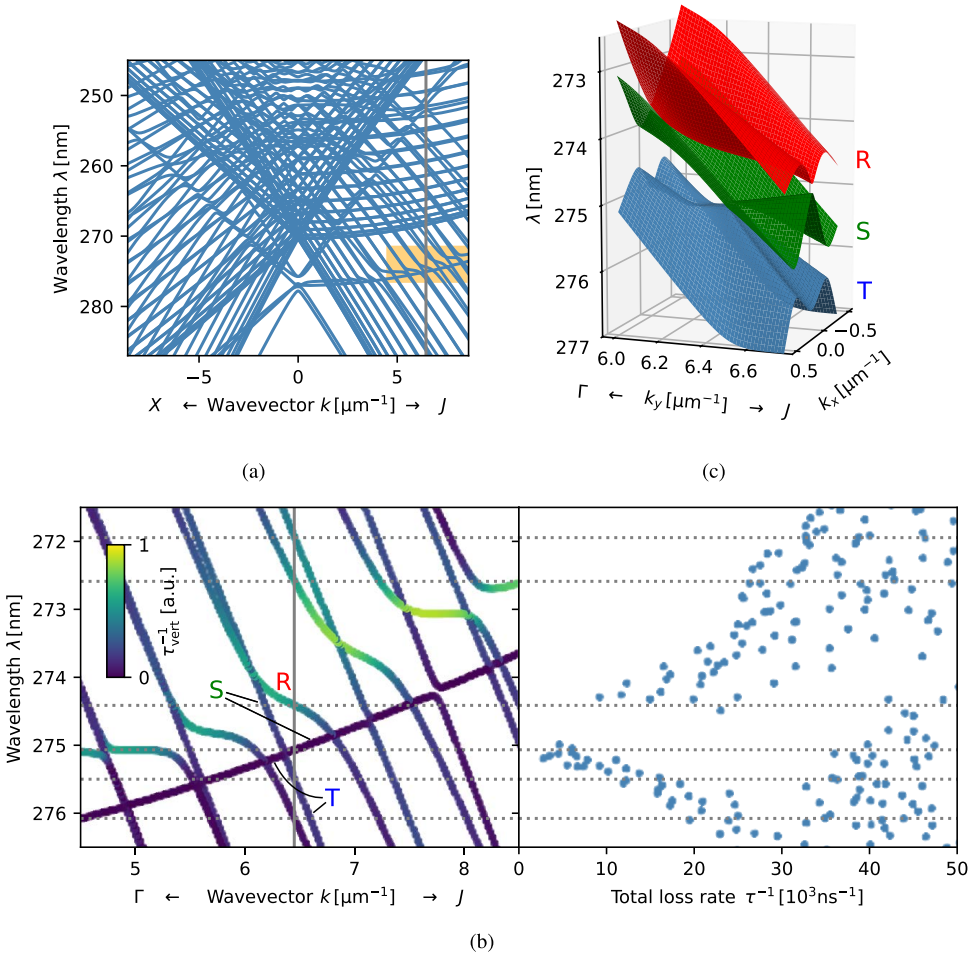

Fig. 10. (a) Band structure of an infinite PCSEL obtained by GME considering the first 20 vertical modes and only the fundamental lateral modes. The vertical solid grey line indicates the offset parameter $\Delta\mathbf{k} = 6.45\ \mu\text{m}^{-1}\hat{e}_y$. (b) Magnification of the band structure (orange region in (a)) depicting avoided crossings (left panel) where vertical losses are color-coded, and eigenvalues of lowest-loss states obtained by finite-area GME (right panel) incorporating said vertical modes for a PCSEL radius of $L = 25\ \mu\text{m}$. Horizontal dotted lines indicate the wavelengths of the infinite system at $\Delta\mathbf{k}$. (c) Three dimensional representation of the bands R, S, and T of the infinite system in the vicinity of $\Delta\mathbf{k}$.

5. Critical discussion of the quantitative correctness of the finite-area GME method

The numerical accuracy of the GME approach for infinite PCSELs has been validated in Section S3 in the Supplement 1 by comparing to the first-principles RCWA method. Additionally, the overall correctness of the finite-area GME framework for domains with periodic boundary conditions was demonstrated in Section S5 of the Supplement 1. However, the quantitative correctness of neither the 3D-CWT nor the GME approach for finite structures with open boundaries can be rigorously assessed, as the computational requirements for first-principles reference methods such as FDTD and FEM would be too excessive for structures with a reasonable number of unit cells. It has to be emphasized that the underlying slowly varying envelope assumption of

Optics EXPRESS

finite-area GME and CWT breaks down for too small structures which would be accessible for FDTD and FEM.

Nevertheless, in this work, we demonstrated that the incorporation of higher-order lateral and vertical modes in finite-area GME simulations results in changes compared to finite-area CWT which correspond to our findings for the infinite system. These changes include wavelength and loss shifts which can be observed in Figs. 4 and 5 due to higher-order lateral modes, as well as low-loss states arising from avoided crossings with higher-order vertical modes.

6. Conclusions

We demonstrated a finite-area GME method for PCSELs that treats higher-order lateral and vertical modes as genuine basis functions and is based on the slowly varying envelope approach of three-dimensional CWT [16,29]. Systematic studies revealed that finite-sized eigenmodes are affected by higher-order waves: an increased splitting of wavelengths and decreasing lateral outcoupling rates of finite-sized modes are observed for increasing numbers of incorporated lateral waves, which are assumed to arise from enhanced in-plane coupling effects. On the other hand, vertical outcoupling rates tend to increase which is attributed to the stronger coupling to leaky modes. The influence of the number of vertical modes on finite-sized eigenmodes might be systematically investigated in further studies.

Incorporating higher-order vertical (waveguide) modes with nodal planes in the cladding into simulations for infinite structures leads to the emergence of band structure replicas with shorter wavelengths. Avoided crossings with low group velocities form where bands approach the band structure corresponding to the fundamental vertical mode. The resulting low lateral losses approximately coincide with bright regions in photoluminescence measurements when pumped below threshold, which actually start to lase above threshold. Finite-area GME simulations incorporating such cladding modes yield low-threshold states for eigenmodes located at avoided crossings, accordingly, which cannot be directly modeled by current CWT formulations. Including vertical modes is also necessary for a quantitative prediction of the dispersion in the vicinity of the Gamma point, and therefore relevant for any PCSEL design with a vertical structure supporting higher-order modes.

Funding. Knut and Alice Wallenberg Foundation (2020.0119).

Acknowledgment. The authors acknowledge their collaborators Sarina Graupeter, Tim Wernicke, and Michael Kneissl at TU Berlin for the material growth development, material characterization and growth of the epitaxial layer structure which was used in the fabrication of the investigated PCSELs.

Disclosures. The authors declare no conflicts of interest.

Data availability. The data that support the findings of this study are available from the corresponding author upon reasonable request.

Supplemental document. See Supplement 1 for supporting content.

References

1. H. Kogelnik and C. V. Shank, "Stimulated emission in a periodic structure," Appl. Phys. Lett. **18**(4), 152–154 (1971).
2. K. Iga, "Surface-emitting laser-its birth and generation of new optoelectronics field," IEEE J. Sel. Top. Quantum Electron. **6**(6), 1201–1215 (2000).
3. S. Noda, M. Yoshida, T. Inoue, *et al.*, "Photonic-crystal surface-emitting lasers," Nat Rev Electr Eng **1**(12), 802–814 (2024).
4. M. Yoshida, S. Katsuno, T. Inoue, *et al.*, "High-brightness scalable continuous-wave single-mode photonic-crystal laser," Nature **618**(7966), 727–732 (2023).
5. M. Imada, S. Noda, A. Chutinan, *et al.*, "Coherent two-dimensional lasing action in surface-emitting laser with triangular-lattice photonic crystal structure," Appl. Phys. Lett. **75**(3), 316–318 (1999).
6. S. Noda, M. Yokoyama, M. Imada, *et al.*, "Polarization mode control of two-dimensional photonic crystal laser by unit cell structure design," Science **293**(5532), 1123–1125 (2001).
7. D. Apaydln, H. Andersson, L. Uhlig, *et al.*, "Deep-UV photonic crystal surface-emitting lasers," Laser & Photonics Reviews **20**(6), e00271 (2026).

Optics EXPRESS

8. S. E. Beck, H. Ryu, L. A. Boczek, *et al.*, "Evaluating UV-C LED disinfection performance and investigating potential dual-wavelength synergy," Water Res. **109**, 207–216 (2017).
9. W. J. Abbey, R. Bhartia, L. W. Beegle, *et al.*, "Deep UV Raman spectroscopy for planetary exploration: The search for in situ organics," Icarus **290**, 201–214 (2017).
10. K. Sakai, E. Miyai, and S. Noda, "Coupled-wave model for square-lattice two-dimensional photonic crystal with transverse-electric-like mode," Appl. Phys. Lett. **89**(2), 021101 (2006).
11. Y. Liang, C. Peng, K. Sakai, *et al.*, "Three-dimensional coupled-wave model for square-lattice photonic crystal lasers with transverse electric polarization: A general approach," Phys. Rev. B **84**(19), 195119 (2011).
12. T. Inoue, R. Morita, M. Yoshida, *et al.*, "Comprehensive analysis of photonic-crystal surface-emitting lasers via time-dependent three-dimensional coupled-wave theory," Phys. Rev. B **99**(3), 035308 (2019).
13. S. Katsuno, T. Inoue, M. Yoshida, *et al.*, "Self-consistent analysis of photonic-crystal surface-emitting lasers under continuous-wave operation," Opt. Express **29**(16), 25118–25132 (2021).
14. I. Vurgaftman and J. Meyer, "Photonic-crystal distributed-feedback quantum cascade lasers," IEEE J. Quantum Electron. **38**(6), 592–602 (2002).
15. I. Vurgaftman and J. Meyer, "Design optimization for high-brightness surface-emitting photonic-crystal distributed-feedback lasers," IEEE J. Quantum Electron. **39**(6), 689–700 (2003).
16. Y. Liang, C. Peng, K. Ishizaki, *et al.*, "Three-dimensional coupled-wave analysis for triangular-lattice photonic-crystal surface-emitting lasers with transverse-electric polarization," Opt. Express **21**(1), 565–580 (2013).
17. M. Yokoyama and S. Noda, "Finite-difference time-domain simulation of two-dimensional photonic crystal surface-emitting laser," Opt. Express **13**(8), 2869–2880 (2005).
18. T. Rylander, P. Ingelström, and A. Bondeson, *Computational Electromagnetics* (Springer, 2013), Chap. 5.
19. J. D. Joannopoulos, S. G. Johnson, J. N. Winn, *et al.*, *Photonic Crystals: Molding the Flow of Light* (Princeton University, 2008), chap. Appendix D.
20. M. Imada, A. Chutinan, S. Noda, *et al.*, "Multidirectionally distributed feedback photonic crystal lasers," Phys. Rev. B **65**(19), 195306 (2002).
21. K. Sakai, E. Miyai, T. Sakaguchi, *et al.*, "Lasing band-edge identification for a surface-emitting photonic crystal laser," IEEE J. Select. Areas Commun. **23**(7), 1335–1340 (2005).
22. L. C. Andreani and D. Gerace, "Photonic-crystal slabs with a triangular lattice of triangular holes investigated using a guided-mode expansion method," Phys. Rev. B **73**(23), 235114 (2006).
23. S. Zanotti, M. Minkov, D. Nigro, *et al.*, "Legume: A free implementation of the guided-mode expansion method for photonic crystal slabs," Comput. Phys. Commun. **304**, 109286 (2024).
24. M. Minkov, I. A. D. Williamson, L. C. Andreani, *et al.*, "Inverse design of photonic crystals through automatic differentiation," ACS Photonics **7**(7), 1729–1741 (2020).
25. B. Lang, P. Sewell, A. Vukovic, *et al.*, "Assessment and extension of rapid design tools for modeling photonic crystal surface-emitting lasers," J. Opt. Soc. Am. B **42**(5), 1123–1130 (2025).
26. L. Persson, M. Riedel, Å. Haglund, *et al.*, "Finite-size effects in photonic-crystal surface-emitting lasers: critical discussion of different approximations," Opt. Express **33**(25), 53098–53116 (2025).
27. D. Apaydl, L. Persson, M. Riedel, *et al.*, "Influence of photonic crystal size and lattice constant on the lasing performance of deep-UV PCSELs," manuscript submitted.
28. P. Strzebonski and K. D. Choquette, "Guided mode expansion analysis of photonic crystal surface emitting lasers," (2021).
29. Y. Liang, C. Peng, K. Sakai, *et al.*, "Three-dimensional coupled-wave analysis for square-lattice photonic crystal surface emitting lasers with transverse-electric polarization: finite-size effects," Opt. Express **20**(14), 15945–15961 (2012).
30. H.-Y. Ryu, M. Notomi, and Y.-H. Lee, "Finite-difference time-domain investigation of band-edge resonant modes in finite-size two-dimensional photonic crystal slab," Phys. Rev. B **68**(4), 045209 (2003).
31. J. D. Joannopoulos, S. G. Johnson, J. N. Winn, *et al.*, *Photonic Crystals: Molding the Flow of Light* (Princeton University, 2008), Chap. 3.
32. K. Sakai, E. Miyai, and S. Noda, "Coupled-wave theory for square-lattice photonic crystal lasers with te polarization," IEEE J. Quantum Electron. **46**(5), 788–795 (2010).
33. B. Witzigmann, F. Römer, M. Martens, *et al.*, "Calculation of optical gain in AlGaN quantum wells for ultraviolet emission," AIP Adv. **10**(9), 095307 (2020).
34. N. A. Sanford, L. H. Robins, A. V. Davydov, *et al.*, "Refractive index study of $Al_xGa_{1-x}N$ films grown on sapphire substrates," J. Appl. Phys. **94**(5), 2980–2991 (2003).
35. J. D. Joannopoulos, S. G. Johnson, J. N. Winn, *et al.*, *Photonic Crystals: Molding the Flow of Light* (Princeton University, 2008), Chap. 2.
36. K. Emoto, T. Koizumi, M. Hirose, *et al.*, "Wide-bandgap gan-based watt-class photonic-crystal lasers," Commun. Mater. **3**(1), 72 (2022).
37. E. Miyai, K. Sakai, T. Okano, *et al.*, "Photonics: Lasers producing tailored beams," Nature **441**(7096), 946 (2006).
38. P. Lalanne and G. M. Morris, "Highly improved convergence of the coupled-wave method for TM polarization," J. Opt. Soc. Am. A **13**(4), 779–784 (1996).
39. L. Li, "Use of fourier series in the analysis of discontinuous periodic structures," J. Opt. Soc. Am. A **13**(9), 1870–1876 (1996).

Optics EXPRESS

40. A. Y. Song, A. R. K. Kalapala, W. Zhou, *et al.*, "First-principles simulation of photonic crystal surface-emitting lasers using rigorous coupled wave analysis," Appl. Phys. Lett. **113**(4), 041106 (2018).
41. D. M. Whittaker and I. S. Culshaw, "Scattering-matrix treatment of patterned multilayer photonic structures," Phys. Rev. B **60**(4), 2610–2618 (1999).
42. F. Xiao, J. Wang, Z. Xiong, *et al.*, "Numerical approximation of slowly varying envelope in finite element electromagnetism: a ray-wave method of modeling multi-scale devices," Opt. Express **33**(6), 12603–12614 (2025).
43. T. Xu, S. Yang, S. V. Nair, *et al.*, "Confined modes in finite-size photonic crystals," Phys. Rev. B **72**(4), 045126 (2005).
44. Y. Chassagneux, R. Colombelli, W. Maineult, *et al.*, "Electrically pumped photonic-crystal terahertz lasers controlled by boundary conditions," Nature **457**(7226), 174–178 (2009).
45. J. D. Joannopoulos, S. G. Johnson, J. N. Winn, *et al.*, *Photonic Crystals: Molding the Flow of Light* (Princeton University, 2008), Chap. 8.